

2D Programmable Photodetectors Based on WSe₂/h-BN/Graphene Heterojunctions

Zhihao Wang, Jialing Jian, Zhengjin Weng, Qianqian Wu, Jian Li, Xingyu Zhou, Wei Kong, Xiang Xu, Liangliang Lin, Xiaofeng Gu, Peng Xiao,* Haiyan Nan,* and Shaoqing Xiao*

Programmable photovoltaic photodetectors based on 2D materials can modulate optical and electronic signals in parallel, making them particularly well-suited for optoelectronic hybrid dual-channel communication. This work presents a programmable non-volatile bipolar semi-floating gate photovoltaic photodetector (SFG-PD) constructed using tungsten diselenide (WSe₂), hexagonal boron nitride (h-BN), and graphene (Gra). By controlling the voltage pulses applied to the control gate, the device generates opposing built-in electric field junctions (p⁺-p and n-p junctions), enabling reversible switching between positive and negative light responses with a rapid response time of up to 2.02 μs. Moreover, the application of this device is demonstrated in dual-channel optoelectronic hybrid communication, offering a practical solution for achieving high-speed, large-capacity, low-loss, and secure multi-channel communication.

1. Introduction

Traditional electronic communication systems face limitations such as bandwidth bottlenecks and low energy efficiency, making it challenging to meet the demands for data transmission speed,

capacity, and latency brought about by the rapid development of artificial intelligence (AI) and big data technologies.^[1] Optoelectronic hybrid dual-channel communication offers a potential solution by leveraging the advantages of optical and electronic signals to achieve high-speed, high-capacity, and low-power data transmission. Programmable photovoltaic photodetectors based on atomically thin 2D materials^[2] can modulate optical and electronic signals in parallel, making them particularly well-suited for such systems.^[3]

Programmable photovoltaic photodetectors based on 2D materials can establish built-in electric field junctions through electrostatic doping, enabling dynamic modulation of the majority of internal carriers. This approach overcomes the limitations

of traditional photovoltaic photodetectors, such as unidirectional built-in electric fields, low light absorption, and fixed carrier transport behaviors.^[4] It also enables the formation of various types of junctions, including p⁺-p,^[5] n-p,^[5] n⁺-n,^[6] and Schottky junctions,^[7] paving the way for the practical use of programmable photovoltaic photodetectors in optoelectronic hybrid communication systems.^[8]

Programmable photovoltaic photodetectors typically rely on electrostatic doping, achieved through continuous or pulsed gating. This approach allows precise control over the direction of the built-in electric field, enabling seamless switching between positive and negative responses. Examples include homojunction-based volatile photovoltaic detectors, such as those made from WSe₂,^[9] BP,^[10] MoTe₂,^[11] and non-volatile devices like MoTe₂.^[6] Compared to volatile photovoltaic photodetectors controlled by continuous gating, non-volatile devices utilizing split gating consume less power.^[6] Among these, non-volatile photovoltaic photodetectors based on a semi-floating gate (SFG) structure stand out due to their well-defined dimensions, extended retention time, rapid response, and cost-effectiveness.^[5,12]

To further enhance the response speed, we developed a programmable non-volatile bipolar semi-floating gate photovoltaic photodetector (SFG-PD) using WSe₂, hexagonal boron nitride (h-BN), and graphene (Gra). The WSe₂ SFG-PD device demonstrates exceptional performance and unique functionality, achieving rapid positive and negative self-driven light (637 nm) responses of 8.77 μs / 2.02 μs and 5.92 μs / 7.80 μs, respectively, under +20 V and -20 V gate voltage pulses. Additionally, the self-driven device exhibits high responsivities of 2.76 A/W and

Z. Wang, J. Jian, Z. Weng, Q. Wu, J. Li, X. Zhou, X. Gu, H. Nan, S. Xiao
Engineering Research Center of IoT Technology Applications (Ministry of Education) School of Integrated Circuits

Jiangnan University
Wuxi 214122, China
E-mail: jnanhaiyan@jiangnan.edu.cn; xiaosq@jiangnan.edu.cn

W. Kong, X. Xu
School of Engineering Westlake University
Hangzhou 310030, China

L. Lin
School of Chemical and Material Engineering
Jiangnan University
Wuxi 214122, China

P. Xiao
Laboratoire Ondes et Matière d'Aquitaine (LOMA)-UMR 5798
CNRS
Talence F-33400, France
E-mail: peng.xiao@u-bordeaux.fr

 The ORCID identification number(s) for the author(s) of this article can be found under <https://doi.org/10.1002/advs.202417300>

© 2025 The Author(s). Advanced Science published by Wiley-VCH GmbH. This is an open access article under the terms of the [Creative Commons Attribution License](#), which permits use, distribution and reproduction in any medium, provided the original work is properly cited.

DOI: 10.1002/advs.202417300

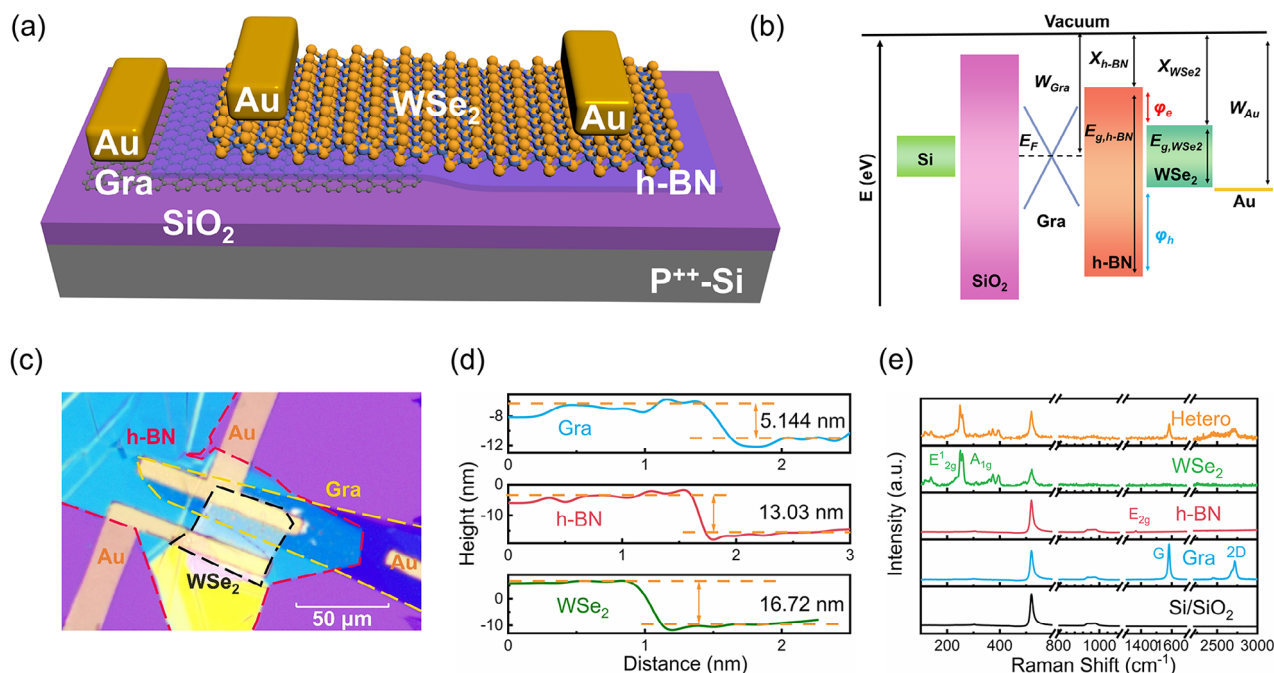


Figure 1. Conceptual illustration and characterization of the WSe₂/h-BN/Gra heterojunction. a) Schematic diagram of the WSe₂/h-BN/Gra semi-floating gate photodetector (WSe₂ SFG-PD). b) Flat energy bands of the Au/WSe₂/h-BN/graphene heterostructure. c) Optical microscope image of the fabricated WSe₂ SFG-PD device. d) Extracted heights of the Gra, h-BN, and WSe₂ flakes corresponding to the blue, orange, and green lines of proposed devices (in Figure S2, Supporting Information). e) Raman spectrum of the WSe₂/h-BN/Gra heterostructure photodetector.

1.63 A/W, high specific detectivity of 7.86×10^{11} Jones and 4.42×10^{11} Jones, low noise equivalent power of 4.76×10^{-15} W/Hz^{1/2} and 8.47×10^{-15} W/Hz^{1/2}, under these two gate voltage pulses, respectively, and excellent retention performance exceeding 2×10^3 s. Furthermore, we utilized the WSe₂ SFG-PD device to convert binary optoelectronic mixed signals into balanced ternary electrical signals in real-time, enabling high-speed, large-capacity, low-loss, and secure dual-channel optoelectronic hybrid communication. This innovative approach positions the WSe₂ SFG-PD as a promising solution for multi-channel communication. Its advanced optoelectronic hybrid communication capabilities provide a practical and efficient means to address the demands for high-speed, high-capacity, and low-power data transmission in the era of AI and big data, paving the way for future advancements in communication technologies.

2. Results and Discussion

2.1. Device Structure and Microscopic Characterization

A schematic diagram of the non-volatile SFG-PD based on the WSe₂/h-BN/Gra heterostructure is depicted in Figure 1a, where WSe₂, h-BN, and Gra flakes serve as the channel, tunneling layer, and SFG, respectively. The corresponding flat band diagram of the WSe₂/h-BN/Gra heterostructure is shown in Figure 1b. Here, $W_{Au} = 5.1$ eV,^[13] $W_{Gra} = 4.6$ eV,^[13] and $W_{WSe_2} = 4.89$ eV are the work functions of Au, graphene, and WSe₂, respectively (as shown in Figure S1, Supporting Information). Additionally, $X_{WSe_2} = 3.5$ – 4.0 eV and $X_{h-BN} = 2$ – 2.3 eV^[13] are the electron affinities of WSe₂ and h-BN, respectively, while the bandgaps

of WSe₂ (E_{g,WSe_2}) and h-BN ($E_{g,h-BN}$) are 1.4 and 5.96 eV,^[5] respectively. The working principle of this structure primarily relies on the band alignment of the heterojunction and the quantum tunneling effect WSe₂, as the channel material, can effectively absorb photons and generate charge carriers, while h-BN, serving as the tunneling layer, allows for the rapid tunneling of charge carriers into the SFG (Gra) under appropriate gate voltage pulses, thereby generating image charge in the channel material and creating a tunable built-in electric field. This design allows for efficient generation and detection of current under illumination, while the non-volatile characteristics enable the photodetector to retain the previous signal state even after being turned off. The fabrication process of the device is described in detail in the experimental section, as shown in Figure S2 (Supporting Information). Figure 1c shows the optical microscope image of a typical non-volatile SFG-PD based on the WSe₂/h-BN/Gra heterostructure, where WSe₂, h-BN, and Gra flakes are indicated by black, red, and yellow dashed lines, respectively. The thickness of WSe₂, h-BN, and Gra was characterized using atomic force microscopy (AFM), with the flake thicknesses measured at 16.72, 13.03, and 5.14 nm, respectively, as shown in Figure 1d (the device image under AFM is shown in Figure S3, Supporting Information). First, single-layer graphene limits its ability to store a significant number of carriers due to its low density of states,^[5] while thicker graphene can cause the h-BN above the heterojunction to fracture. Therefore, the selection of graphene thickness is crucial. After extensive experiments, a multilayer graphene thickness of 5.14 nm was chosen as the floating gate.^[14] Additionally, h-BN, which has a wide bandgap (≈ 6 eV), is commonly used as a dielectric tunneling layer. For 2D material floating gate de-

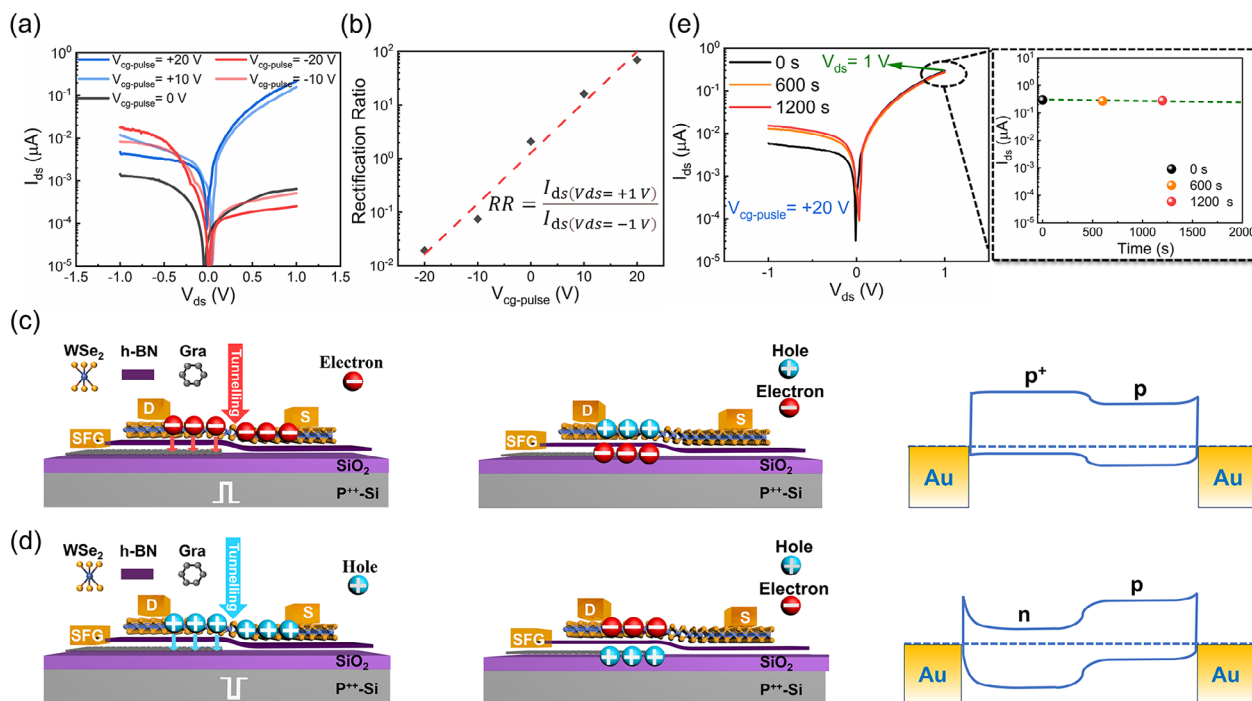


Figure 2. Implementation of non-volatile p^+ -p/n-p junctions in the $WSe_2/h\text{-BN}/\text{Gra}$ heterojunction. a) Semi-logarithmic I_{DS} - V_{DS} curves of WSe_2 under different gate voltage pulses applied to Si. b) Extraction and fitting of the rectification ratio of WSe_2 corresponding to different gate voltage pulses based on the proposed device. c) Operation diagram of the WSe_2 SFG-PD device under positive V_{cg} applied and released to the Si control gate (left), tunneling charges in the SFG layer inducing mirror charge formation in the channel material (middle), and the energy band diagram of the p^+ -p homojunction device (right). d) Operation diagram of the WSe_2 SFG-PD device under negative V_{cg} applied and released to the Si control gate (left), tunneling charges in the SFG layer inducing mirror charge formation in the channel material (middle), and the energy band diagram of the n-p homojunction device (right). e) Time-dependent semi-logarithmic I_{DS} - V_{DS} curve of WSe_2 under a +20 V gate voltage pulse applied on Si. Inset: Fitting curve of I_{DS} as a function of time for WSe_2 under a +20 V gate voltage pulse with $V_{DS} = +1$ V applied to Si.

vices, the tunneling layer thickness is typically set between 10 and 20 nm.^[15] Considering this, the thickness of the h-BN flake was chosen to be ≈ 13.03 nm to achieve ultrafast operation speed and excellent retention performance. Figure 1e displays the Raman spectrum of the $WSe_2/h\text{-BN}/\text{Gra}$ heterostructure. The WSe_2 flakes exhibit two distinct peaks at 250 and 258 cm^{-1} , corresponding to the in-plane (E_{1g}) and out-of-plane (A_{1g}) vibrational modes, respectively. The characteristic peak of h-BN is located at 1366 cm^{-1} , corresponding to the in-plane (E_{2g}) vibrational mode. Furthermore, the peaks at 1582 cm^{-1} (G) and 2716 cm^{-1} (2D) are two typical characteristic peaks of multi-layer graphene. This phenomenon shows that no additional discernible Raman peaks were observed, affirming the absence of defects introduced during the fabrication process. In addition, to further assess the structural properties and quality of the WSe_2 , h-BN, and Gra materials, X-ray diffraction (XRD) measurements were conducted. The results presented in Figure S4 (Supporting Information) reveal that these materials display an ordered layered structure with well-aligned interlayer stacking, minimal defects, and high crystallinity, further confirming their superior quality characteristics.

2.2. Device Performance and Mechanism

The electrical characteristics were evaluated using a Si substrate as the control gate (V_{cg}) for channel programming and erasing.

In this study, the pulse duration was uniformly set to 1 s to ensure saturation at a specific V_{cg} pulse level, with Gra serving as the storage charge in the SFG. As shown in the output curve of Figure 2a, a pulsed gate voltage of $V_{cg-pulse} = \pm 20$ V (Per increment $|10|$ V) was applied to the Si substrate, resulting in opposite rectifying characteristics in the WSe_2 SFG-PD device under the $\pm V_{cg-pulse}$. The fitting curves of the rectification ratio under different $V_{cg-pulse}$ conditions show that the rectification ratio exhibits an almost linear dependence on the gate $V_{cg-pulse}$, specifically being $\approx 10^{-2}$ at $V_{cg-pulse} = -20$ V and $\approx 10^2$ at $V_{cg-pulse} = +20$ V in Figure 2b. This indicates that the modulation levels and mechanisms for different $\pm V_{cg-pulse}$ may be similar, the effect observed in the WSe_2 SFG-PD device is attributed to charge injection/capture in the SFG and the channel heterojunction configurations (p^+ -p and n-p).

As shown in Figure 2c, during the application of $V_{cg} > 0$ V, electrons rapidly accumulate in WSe_2 and tunnel through the h-BN layer to reach the SFG, where they are stored (left image). After transitioning from $V_{cg} > 0$ V to $V_{cg} = 0$ V (where a complete positive gate pulse has been formed), the accumulated electrons in WSe_2 disappear, and the stored tunneling electrons in the SFG induce image charge holes in the WSe_2 above (middle image). Consequently, holes accumulate in the portion of WSe_2 above the SFG, lowering the Fermi level and forming a p^+ -p junction, as depicted in the band structure in the right panel of Figure 2c. Similarly, as shown in Figure 2d, during the application of $V_{cg} < 0$ V, holes rapidly accumulate in WSe_2 and tunnel through the

h-BN layer to reach the SFG, where they are stored (left image). After transitioning from $V_{cg} < 0$ V to $V_{cg} = 0$ V (where a complete negative gate pulse has been formed), the accumulated holes in WSe_2 disappear, and the stored tunneling holes in the SFG induce image charge electrons in the WSe_2 above (middle image). Therefore, electrons accumulate in the portion of WSe_2 above the SFG, raising the Fermi level and forming an n-p junction, as depicted in the band structure in the right panel of Figure 2d. If Gra is grounded, the rectifying characteristics of WSe_2 will disappear. Notably, charge modulation within the h-BN/Gra van der Waals (vdWs) floating gate can be achieved at a speed of 20 ns through the improved Fowler-Nordheim tunneling effect.^[16] To characterize the device stability, as shown in Figure 2e, the output characteristics of the device were tested at 0, 600, and 1200 s after applying $V_{cg-pulse} = +20$ V. It is evident that I_{DS} ($V_{DS} = -1$ V) gradually increases over time, attributed to a small number of electrons in the portion of WSe_2 above the SFG tunneling through h-BN and being captured by defects in SiO_2 , releasing slowly.^[17] Similarly, after applying $V_{cg-pulse} = -20$ V, a small number of holes in the portion of WSe_2 above the SFG tunnel through h-BN when the negative gate pulse is applied and are captured by defects in SiO_2 , releasing slowly.^[17] As a result, I_{DS} ($V_{DS} = -1$ V) gradually decreases over time (as shown in Figure S5, Supporting Information). The changes in I_{DS} ($V_{DS} = 1$ V) over time for $V_{cg-pulse} = \pm 20$ V are fitted in Figure 2e and Figure S5 (Supporting Information), clearly indicating that the carriers stored in the SFG can be retained for over 2000 s. To further evaluate the stability of the device, we tested the performance of the WSe_2 SFG-PD device over 1000 cycles of periodic gate voltage pulses. As shown in Figure S6a (Supporting Information), the device maintains stable and reversible light response characteristics under these periodic gate voltage pulses, indicating that it does not exhibit significant performance degradation during repeated operation. This behavior demonstrates that the WSe_2 SFG-PD device possesses excellent operational stability, capable of withstanding long-term periodic operation without substantial performance decay. Furthermore, Figure S6b (Supporting Information) presents the error bar curve extracted from Figure S6a (Supporting Information), where it is clear that, after 1000 gate voltage pulses, the performance fluctuations of the device remain within a narrow range, further confirming the high stability and reliability of the device. Based on these test results, we conclude that the device demonstrates high durability and long-term stability, making it well-suited to withstand frequent operations and environmental changes in practical applications.

To assess the quality of the device, it is necessary to evaluate the number of recombination centers and trap states through the carrier transport process in the homojunction. The transport in the homojunction can be fitted using the Shockley diode equation

$$I_D = \frac{nV_T}{R_s} W \left[\frac{I_0 R_s}{nV_T} \exp \left(\frac{V_{DS} + I_0 R_s}{nV_T} \right) \right] - I_0 \quad (1)$$

here, I_0 is the reverse saturation current, $V_T = k_B T/q$ is the thermal voltage at temperature T , R_s is series resistance, where k_B is the Boltzmann constant, q is the electronic charge, W is the Lambert W function, and n is the ideality factor.^[5] The ideality factor n describes the diffusion and recombination behavior of charge

carriers as they traverse the depletion region. It is commonly used to characterize the imperfections in real transistor junctions, as recombination centers are invariably present in these regions. It typically ranges from 1 to 2 depending on the fabrication process, interfaces, and semiconductor materials. For an “ideal” diode, there are no recombination centers in the junction depletion region, thus the ideality factor n equals 1. From the I_{DS} - V_{DS} curve (see Figure S7, Supporting Information), we calculated $n = 1.13$ for the p⁺-p junction and $n = 1.24$ for the n-p junction. Here, we conclude that the charge carriers in the p⁺-p junction at $V_{cg-pulse} = +20$ V and the n-p junction at $V_{cg-pulse} = -20$ V are predominantly driven by diffusion, with a mixture of diffusion and recombination processes during transport. Since the ideality factor n in the p⁺-p junction is closer to 1 than that in the n-p junction, this indicates that there are fewer recombination centers and trap states in the p⁺-p junction.

Previous studies^[18] have shown that at lower gate voltages, direct tunneling dominates, while at higher gate voltages, the Fowler-Nordheim (F-N) mechanism governs the tunneling process. The current equation for F-N tunneling can be expressed as follows:^[18]

$$I(V) = \frac{A_{eff} q^3 m V^2}{8\pi h \phi_B d^2 m^*} \exp \left(\frac{-8\pi \sqrt{2m^*} \phi_B^{3/2} d}{3hqV} \right) \quad (2)$$

where V , A_{eff} , ϕ_B , q , m , m^* , d , and h represent the applied voltage, effective contact area, barrier height, electron charge, mass of a free electron, mass of tunneling electrons in h-BN ($m^*/m = 0.26$),^[19] thickness of the tunneling layer, and Planck's constant, respectively. The equation can be rewritten as:

$$\ln \left(\frac{I(V)}{V^2} \right) = \ln A - B \cdot \frac{1}{V} \quad (3)$$

where

$$A = \frac{A_{eff} q^3 m}{8\pi h \phi_B d^2 m^*}, B = \frac{8\pi \sqrt{2m^*} \phi_B^{3/2} d}{3hq} \quad (4)$$

The F-N tunneling current was tested by applying voltage to the drain and SFG electrodes to illustrate the carrier tunneling mechanism. Figure S8a (Supporting Information) shows the test results, which indicate that direct tunneling dominates when $V_{DS} \leq 5.1$ V, while F-N tunneling prevails when $V_{DS} > 5.1$ V. Additionally, the inset shows a schematic structure of the tested device. Figure S8b (Supporting Information) displays the F-N plot of the I - V curves obtained from the tests, where the linear relationship indicates that the F-N tunneling mechanism dominates in our device.^[20]

2.3. Reconfigurable Photovoltaic Characteristics

Further exploration was conducted on the photovoltaic properties of the WSe_2 SFG-PD with reconfigurable light response. Figure 3a shows the measured photocurrent at $V_{cg-pulse} = +20$ V, 0 V bias, and at different wavelengths. Under illumination of visible light (447 and 637 nm) and near-infrared light (940 nm),

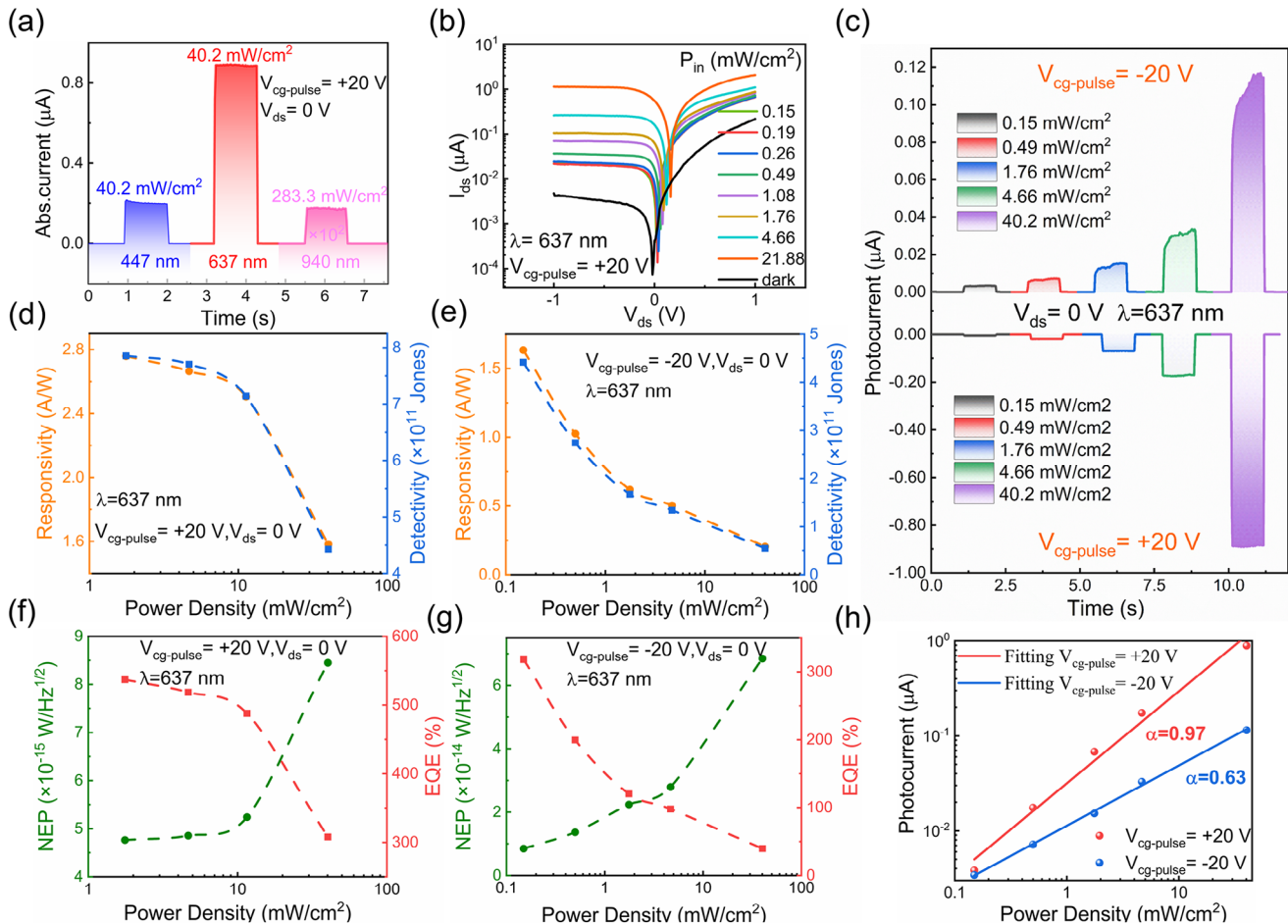


Figure 3. Reconfigurable photovoltaic characteristics in the WSe₂ SFG-PD device. a) Measurement of the switchable electro-optical response of the WSe₂ SFG-PD device at different operating wavelengths under varying incident light powers and at 0 V bias. b) Semi-logarithmic output curves under different input optical powers (P_{in}) with a +20 V voltage pulse applied to Si substrate at 637 nm and 0 V bias. c) Optical response of the WSe₂ SFG-PD structure under a ± 20 V voltage pulse on Si substrate at 637 nm illumination, 0 V bias, with power switching from 0.038 to 10.23 μ W. d,e) Photodetector performance of the device at $V_{cg-pulse} = \pm 20$ V, 0 V bias, and 637 nm, corresponding to responsivity (R) and detectivity (D^*). f,g) Photodetector performance of the device at $V_{cg-pulse} = \pm 20$ V, 0 V bias, and 637 nm, corresponding to noise equivalent power (NEP) and external quantum efficiency (EQE). h) Fitting relationship between photocurrent and optical intensity under $V_{cg-pulse} = \pm 20$ and 0 V bias at 637 nm.

the device exhibits a significantly higher photocurrent at 637 nm compared to other wavelengths, even at lower input power (Figure S9, Supporting Information). Therefore, the following experiments were all conducted under 637 nm light illumination. The band alignment in the WSe₂ channel facilitates the formation of p⁺-p or n-p homojunctions under $\pm V_{cg-pulse}$ tuning, resulting in significant photovoltaic effects with reversed built-in electric fields. Therefore, under 637 nm laser illumination, both reconstructive rectifying behavior and reversible positive/negative photovoltaic behavior can be observed, as shown in Figure 3b and Figure S10 (Supporting Information). Figure 3c shows the dynamic light response at 0 V bias with $V_{cg-pulse} = \pm 20$ V, demonstrating fast self-driven photocurrents with opposite signals for the two modes (p⁺-p and n-p junctions), reaching photocurrents (I_{ph}) of up to 0.89 and 0.12 μ A under 10.23 μ W laser illumination, and switch ratios (I_{on}/I_{off}) of 1600 and 200. This indicates that the current change in the switch state of the detector is significant, usually reflecting good sensitivity

and responsiveness. Moreover, Figure 3d,e shows the responsivity of the proposed device is ≈ 2.76 and 1.63 A/W under $V_{cg-pulse} = \pm 20$ and 0 V bias, while the detectivity is 7.86×10^{11} and 4.42×10^{11} Jones, respectively. The device's higher responsivity exceeds that of similar SFG-PD devices.^[6] When $V_{cg-pulse} = +20$ and at 1 V bias, the device exhibits maximum responsivity and detectivity of 292.20 A/W and 4.16×10^{12} Jones (as shown in Figure S11a, Supporting Information), indicating its excellent ability to detect weak light signals. To further test the signal-to-noise ratio, we measured the noise equivalent power (NEP) of the device. Figure 3f,g displays the NEP (left axis) and external quantum efficiency (EQE) (right axis) under $V_{cg-pulse} = \pm 20$ and 0 V bias. The noise equivalent powers are 4.76×10^{-15} W/Hz^{1/2} and 8.47×10^{-15} W/Hz^{1/2}, while the external quantum efficiencies are 537% and 318%, respectively. When $V_{cg-pulse} = +20$ and at 1 V bias, the device achieves minimum noise equivalent power and maximum external quantum efficiency of 8.99×10^{-16} W/Hz^{1/2} and 56 900% (as shown in Figure S11b, Supporting Information), demonstrat-

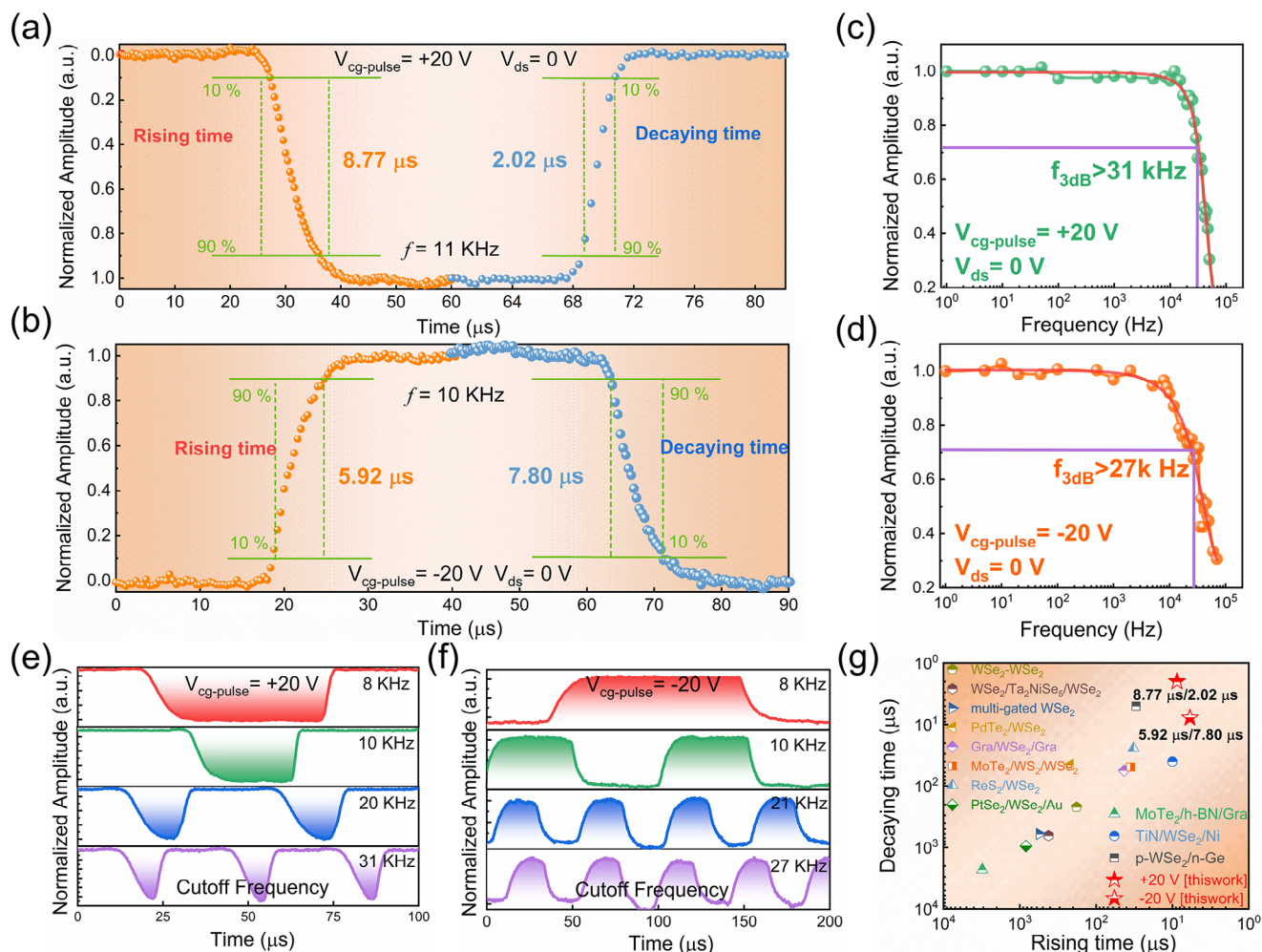


Figure 4. Electro-optical response of the WSe₂ SFG-PD device under 637 nm illumination, with $V_{cg-pulse} = \pm 20$ and 0 V bias. a) Rise time and fall time of the WSe₂ SFG-PD under $V_{cg-pulse} = +20$ and 0 V bias. b) Rise time and fall time of the WSe₂ SFG-PD under $V_{cg-pulse} = -20$ and 0 V bias. Variation of normalized photocurrent in the WSe₂ SFG-PD device with laser modulation frequency under c) $V_{cg-pulse} = +20$ and 0 V bias. d) $V_{cg-pulse} = -20$ and 0 V bias. Normalized optical response characteristics of the WSe₂ SFG-PD to different frequency pulse signals under e) $V_{cg-pulse} = +20$ and 0 V bias. f) $V_{cg-pulse} = -20$ and 0 V bias. g) Comparison of response times of different types of WSe₂ heterostructure photodetectors.

ing its exceptional capability to convert light signals into electrical signals.

We can derive the relationship between photocurrent and light intensity, as shown in Figure 3h. We fitted the data using a power-law equation of the form $I_{ph} = cP^\alpha$. For the device, the α value lies between 0 and 1; the closer α is to 1, the fewer trap states are present in the material, resulting in less loss of carriers due to recombination, with the photoconductive effect dominating the photocurrent. Conversely, the closer α is to 0, the more trap states are present, causing the photocurrent to be determined by the photogating effect.^[21] When the α values for the two different homojunctions (p⁺-p and n-p) generated at $V_{cg-pulse} = \pm 20$ V were 0.97 and 0.63, respectively, it indicates that the device's photocurrent is dominated by the photoconductive effect in both modes. The α value for the p⁺-p junction mode is greater than that for the n-p junction mode, indicating that there are fewer trap states in the p⁺-p junction mode, leading to less carrier loss during recombination. This is consis-

tent with our conclusions drawn from the ideality factors in both modes.

The response bandwidth is a key performance indicator directly related to the response speed of the photodetector. The response speed is a key advantage of the WSe₂ SFG-PD device, reflecting its ability to track rapidly switching optical signals. Here, we use a 637 nm laser irradiation setup to characterize the time-dependent optical response behavior. The rise time (τ_r) and decay time (τ_d) are defined as the time taken for the photocurrent to rise from 10% to 90% of its peak value or to decay from 90% to 10%. Figure 4a shows the optical response times $\tau_r = 8.77$ μ s and $\tau_d = 2.02$ μ s at $V_{cg-pulse} = +20$ V with a 0 V bias. Figure 4b displays the optical response times $\tau_r = 5.92$ μ s and $\tau_d = 7.80$ μ s at $V_{cg-pulse} = -20$ V with a 0 V bias. It is evident that the response speeds under the built-in electric fields of the two different modes (p⁺-p and n-p junctions) are very fast and quite similar. This can be attributed to the introduction of a sacrificial Se layer between Au and WSe₂ to form vdWs contacts (as shown in Figure S12,

Supporting Information), avoiding defects at the electrode interface made by conventional metal deposition methods, and the limitation of Fermi level pinning. The reduction of defects at the electrode interface decreases the impact of lattice scattering at the metal-semiconductor contact, thereby enhancing the speed of carrier collection. Additionally, the vdWs contact formed between WSe₂ and h-BN also reduces lattice scattering at the interface, accelerating the migration speed of photogenerated carriers. On the other hand, the wide depletion region in WSe₂ and the enhanced built-in electric field can accelerate the rapid separation of photogenerated carriers. Furthermore, the essence of the built-in electric field in this device is the generation of image charges in the WSe₂ above due to the stored tunneling charges in the SFG. This electrostatic doping does not introduce defect states into the channel material during doping, as with methods like ion implantation, thus reducing losses and scattering effects due to defect states within WSe₂. Furthermore, we investigate the frequency response of the photodetector by modulating the frequency of the incident light signal. The normalized response of the photodetector to pulsed 637 nm laser over a wide frequency range of 1 Hz–100 kHz is shown in Figure 4c,d. The cutoff frequency is defined as the frequency at which the output signal decreases to –3 dB of the initial output signal as the pulse laser frequency increases. In the case of our WSe₂ SFG-PD device, the cutoff frequency was found to be >31 kHz at $V_{\text{cg-pulse}} = +20$ V and >27 kHz at $V_{\text{cg-pulse}} = -20$ V. Figure 4e,f shows the rapid and consistent switching of photocurrent in the WSe₂ SFG-PD device under different switching frequencies at $V_{\text{cg-pulse}} = \pm 20$ V. This reveals the capability of the photodetector to detect ultrafast optical signals and operate at high frequencies with good stability and reproducibility. However, the device's response degrades at higher frequencies. Figure 4g illustrates the comparison of the response speed performance of the WSe₂ SFG-PD device developed in this study with that of other previously reported WSe₂ composite-structure photodetectors. The device achieves a maximum response speed of 2.02 μs under 637 nm illumination, surpassing the response speed of existing composite-structure WSe₂ photodetectors,^[6,22,23] further highlighting the significant advantages of the WSe₂ SFG-PD device in practical applications.

At the same time, we investigated the effect of different thicknesses of WSe₂ on the performance of this structural device and observed some interesting phenomena. Here, we fabricated WSe₂ SFG-PD devices with three thickness categories: thin (below 10 nm), medium (10–30 nm), and thick (over 30 nm), and tested the semi-logarithmic $I_{\text{DS}}-V_{\text{DS}}$ curves of these devices under different gate pulses. The rectifying behavior of WSe₂ devices varies significantly with thickness and applied voltage. For thin WSe₂ devices (Figure S13a, Supporting Information), a positive pulse ($V_{\text{cg-pulse}} > 0$ V) leads to an intensified rectifying effect, achieving a ratio near 10^3 , while a negative pulse ($V_{\text{cg-pulse}} < 0$ V) results in a diminishing rectifying effect, exhibiting low-pass behavior. In medium-thickness WSe₂ devices (Figure S14a, Supporting Information), a positive pulse reveals a clear forward rectification effect with a ratio approaching 10^2 , whereas a negative pulse displays a strong reverse rectification effect with a ratio $\approx 10^{-2}$, enabling both positive and negative light responses suitable for dual-channel communication. Thick WSe₂ devices (Figure S15a, Supporting Information) show a progressive reduction in rectifying effect under positive pulses, leading to high-

pass behavior, but maintain a robust rectifying effect with a negative pulse, achieving a ratio close to 10^{-3} . Based on the experimental observations, we conclude that the Fermi level of WSe₂ shifts downward as the thickness of the flakes increases, with thinner WSe₂ exhibiting n-type characteristics.^[24] The channel region of thinner WSe₂ experiences a stronger influence from charged interface impurities, which suppresses hole conduction and results in n-type behavior. As the thickness increases, these charged impurities become screened, allowing WSe₂ to display intrinsic properties. Additionally, the density of states increases, leading to a reduction in the Schottky barrier. This shift allows the Fermi level of WSe₂ to align more closely with that of the metal. Therefore, we select WSe₂ flakes with a thickness of 10–30 nm to serve as the channel for dual-channel communication devices.

2.4. Dual-Channel Photoelectric Hybrid Communication

Recognizing the importance of programmable photovoltaic photodetectors in communication, we applied the WSe₂ SFG-PD device in optoelectronic hybrid communication using a dual-channel parallel time-interleaved mode. Using the unique functionalities of the device's special structure, we have realized the real-time output of binary optoelectronic mixed input signals as balanced ternary electrical signals. The analog electrical signals output by the device are then converted into digital electrical signals through computer programming, which are subsequently transformed into ASCII and Unicode, ultimately resulting in Chinese characters, as shown in Figure 5a. Using the WSe₂ SFG-PD as a receiver for optical and electrical signals, we synchronized the collection of the 637 nm laser's optical pulse signal and a voltage pulse signal with an amplitude of ± 20 V lasting 5 ms. This resulted in the output of a balanced ternary electrical signal data stream through the output photocurrent (Regulation: A positive direction of the output photocurrent greater than $|10|$ nA is considered logic '1', a value less than $|10|$ nA is considered logic '0', and a negative direction of the output photocurrent signal greater than $|10|$ nA is considered logic '-1'). For example, when the WSe₂ SFG-PD device receives a continuous voltage pulse signal of –20 V for 5 ms, it forms an n-p junction. At the same time, when the optical pulse signal illuminates the junction region of the device, the built-in electric field causes the device to output a photocurrent that is positive and greater than $|10|$ nA, which is considered as logic "1". However, when the WSe₂ SFG-PD device receives a continuous voltage pulse signal of +20 V for 5 ms, it forms a p⁺-p junction. At the same time, when the optical pulse signal illuminates the junction region of the device, the built-in electric field of the p⁺-p junction, which is oriented opposite to that of the previous n-p junction, causes the device to output a photocurrent that is negative and greater than $|10|$ nA, which is considered as logic "-1". In the absence of illumination, the device outputs a current less than $|10|$ nA, which is regarded as logic "0". Therefore, by inputting specific optical pulse signals and electrical pulse signals to the device, it is possible to obtain specific balanced ternary data streams (such as "6C5F" and "5357"). Subsequently, the balanced ternary information is converted into binary information through programming, then transformed into the corresponding numbers and letters based on ASCII code, and

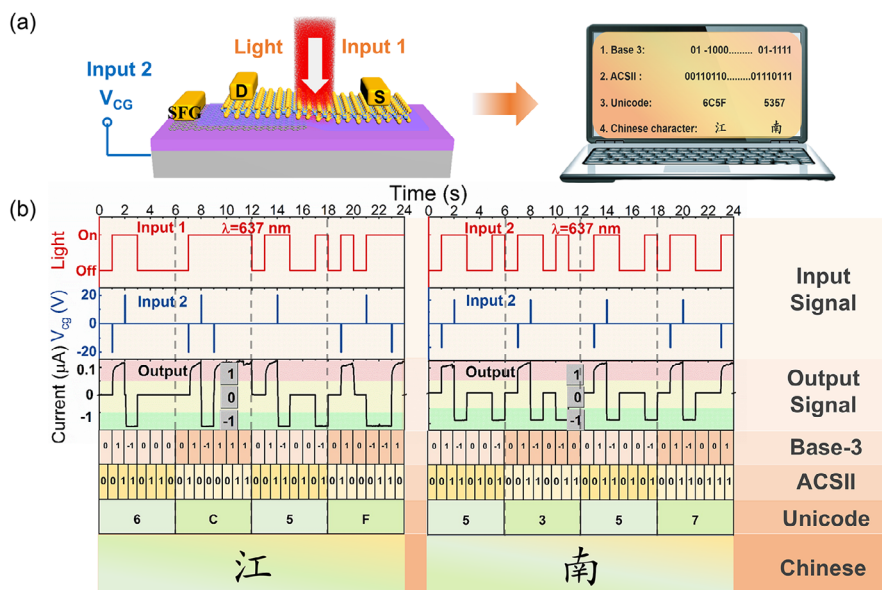


Figure 5. Dual-channel optoelectronic hybrid communication. a) Schematic illustration of dual-channel optoelectronic hybrid communication based on the WSe₂ SFG-PD device. b) This dual-channel optoelectronic hybrid communication system transmits input and output signals containing information streams “6C5F” and “5357” and decodes Chinese characters through Unicode encoding.

finally converted into Chinese characters via Unicode, as shown in Figure 5b. Thus, the WSe₂ SFG-PD device, due to its high-speed response and excellent safety, shows great promise in the field of optical-electrical hybrid communication.

3. Conclusion

By leveraging the unique properties of 2D materials, we designed and fabricated the WSe₂ SFG-PD device by stacking 2D layered structures of WSe₂, h-BN, and graphene. By manipulating the voltage pulses of the back gate, charge carriers can be stored and erased in the graphene floating gate. Using this approach, we successfully achieved a programmable non-volatile self-driven photodetector with ultra-fast response/recovery speeds (8.77 μs / 2.02 μs and 5.92 μs / 7.80 μs), high responsivity (2.76 A/W and 1.63 A/W), high specific detectivity (7.86 × 10¹¹ Jones and 4.42 × 10¹¹ Jones), low noise equivalent power (4.76 × 10⁻¹⁵ W/Hz^{1/2} and 8.47 × 10⁻¹⁵ W/Hz^{1/2}), external quantum efficiency (537% and 318%), and excellent retention performance (>2 × 10³ s). In addition, the device is capable of generating relatively symmetric, oppositely directed built-in electric fields (p⁺-p/n-p junctions). Based on this, we achieved dual-channel optoelectronic hybrid communication by generating balanced ternary electrical signals, enabling high speed, large capacity, low loss, and high security. This demonstrates that the WSe₂ SFG-PD device offers a fast, effective, and convenient new option for optoelectronic hybrid communication.

4. Experimental Section

Device Fabrication: SiO₂/Si (with 300 nm SiO₂ grown on a p⁺-doped Si substrate) was chosen as the substrate. In the initial step, the substrate was first cleaned ultrasonically in acetone, ethanol, and deionized water for 5 min, followed by nitrogen flow drying to remove surface contaminants, ensuring a smooth and even surface. Next, the 2D materials were trans-

ferred onto a designated transfer platform. All 2D material flakes (WSe₂, h-BN, and graphene) were mechanically exfoliated from bulk crystals using polydimethylsiloxane (PDMS). Using a dry transfer technique, in a typical process, graphene flakes were first exfoliated onto a silicon wafer coated with a 300 nm thick layer of thermally oxidized SiO₂. Then, h-BN flakes were transferred onto a transparent PDMS film using adhesive tape and aligned on the graphene flakes with the aid of an optical microscope. By applying gentle pressure, the h-BN was separated from the PDMS film and transferred onto the graphene. Similarly, the WSe₂ layer was aligned and transferred onto the h-BN (with some regions of WSe₂ above graphene and others without). Subsequently, the materials on the substrate and the device were annealed in a nitrogen atmosphere at 250 °C for 3 h to remove interfacial impurities and achieve vdWs contacts between the layers. Finally, using a UV maskless lithography system (Suzhou TuoTuo Technology Co., Ltd.), Se/Au (5 nm/50 nm) electrodes were fabricated via metallic thermal evaporation, and the device was annealed in a vacuum environment at 210 °C (4 × 10⁻⁴ Pa) for 6 h to remove the sacrificial Se layer, resulting in the WSe₂ SFG-PD device.

Characterization and Electrical Testing: Atomic force microscopy (AFM) using the Dimension Fast Scan AFM from BRUKER was employed to characterize the thickness of the 2D materials (WSe₂, h-BN, and graphene). Raman spectra were collected using Raman microscope system (the Renishaw InVia) under 532 nm laser excitation. The optical response characteristics of the WSe₂ SFG photodetector at different wavelengths of the laser system were measured in ambient conditions, both in darkness and under illumination, using a Keithley 2634 B analyzer. An optical attenuator and power meter were used to control and record the light intensity.

Supporting Information

Supporting Information is available from the Wiley Online Library or from the author.

Acknowledgements

Z.H.W. and J.L.J. contributed equally to this work. This work was partially supported by the National Nature Science Foundation under

Grants 62074070 and 52004102, the Natural Science Foundation of Jiangsu Province, China under Grants BK20221534, the Postgraduate Research & Practice Innovation Program of Jiangsu Province, China under KYCX23_2448, the 111 Project under Grant B23008. This project received funding from the European Union's Horizon Europe research and innovation programme under the Marie Skłodowska-Curie grant agreement No. 101107155 (Carmen). Views and opinions expressed are however those of the author(s) only and do not necessarily reflect those of the European Union or the European Research Executive Agency. Neither the European Union nor the granting authority can be held responsible for them. We sincerely appreciate the support of the Service Center for Physical Sciences at Westlake University during the testing process.

Conflict of Interest

The authors declare no conflict of interest.

Data Availability Statement

The data that support the findings of this study are available from the corresponding author upon reasonable request.

Keywords

2D photodetector, fast response, non-volatile, programmable, semi-floating gate

Received: December 23, 2024

Revised: February 26, 2025

Published online: April 4, 2025

- [1] a) D. Bertozzi, G. Dimitrakopoulos, J. Flich, S. Sonntag, *Design Automation Embedded Syst.* **2015**, 19, 59; b) C. Wang, Y. He, F. R. Yu, Q. Chen, L. Tang, *IEEE Commun. Surveys Tutorials* **2018**, 20, 7.
- [2] a) K. S. Novoselov, V. I. Fal'ko, L. Colombo, P. R. Gellert, M. G. Schwab, K. Kim, *Nature* **2012**, 490, 192; b) M. Yankowitz, S. W. Chen, H. Polshyn, Y. X. Zhang, K. Watanabe, T. Taniguchi, D. Graf, A. F. Young, C. R. Dean, *Science* **2019**, 363, 1059; c) J. Wu, Z. Yang, C. Qiu, Y. Zhang, Z. Wu, J. Yang, Y. Lu, J. Li, D. Yang, R. Hao, E. Li, G. Yu, S. Lin, *Nanoscale* **2018**, 10, 8023; d) J. Wu, M. Wei, J. Mu, H. Ma, C. Zhong, Y. Ye, C. Sun, B. Tang, L. Wang, J. Li, X. Xu, B. Liu, L. Li, H. Lin, *ACS Nano* **2021**, 15, 15982; e) Z. Q. Li, X. Y. Liu, C. L. Zuo, W. Yang, X. S. Fang, *Adv. Mater.* **2021**, 33, 2103010; f) X. M. Zhang, H. Y. Nan, S. Q. Xiao, X. Wan, X. F. Gu, A. J. Du, Z. H. Ni, K. Ostrikov, *Nat. Commun.* **2019**, 10, 598; g) L. Liu, T. T. Li, L. Ma, W. S. Li, S. Gao, W. J. Sun, R. K. Dong, X. L. Zou, D. X. Fan, L. W. Shao, C. Y. Gu, N. X. Dai, Z. H. Yu, X. Q. Chen, X. C. Tu, Y. F. Nie, P. Wang, J. L. Wang, Y. Shi, X. R. Wang, *Nature* **2022**, 605, 69; h) J. L. Wang, Q. Yao, C. W. Huang, X. M. Zou, L. Liao, S. S. Chen, Z. Y. Fan, K. Zhang, W. Wu, X. H. Xiao, C. Z. Jiang, W. W. Wu, *Adv. Mater.* **2016**, 28, 8302; i) T. Li, W. Guo, L. Ma, W. Li, Z. Yu, Z. Han, S. Gao, L. Liu, D. Fan, Z. Wang, Y. Yang, W. Lin, Z. Luo, X. Chen, N. Dai, X. Tu, D. Pan, Y. Yao, P. Wang, Y. Nie, J. Wang, Y. Shi, X. Wang, *Nat. Nanotechnol.* **2021**, 16, 1201; j) N. Li, Q. Q. Wang, C. Shen, Z. Wei, H. Yu, J. Zhao, X. B. Lu, G. L. Wang, C. L. He, L. Xie, J. Q. Zhu, L. J. Du, R. Yang, D. X. Shi, G. Y. Zhang, *Nat. Electron.* **2020**, 3, 711.
- [3] a) F. H. L. Koppens, T. Mueller, P. Avouris, A. C. Ferrari, M. S. Vitiello, M. Polini, *Nat. Nanotechnol.* **2014**, 9, 780; b) C. Xie, C. Mak, X. M. Tao, F. Yan, *Adv. Funct. Mater.* **2017**, 27, 41; c) N. J. Huo, G. Konstantatos, *Adv. Mater.* **2018**, 30, 27; d) F. K. Wang, Y. Zhang, Y. Gao, P. Luo, J. W. Su, W. Han, K. L. Liu, H. Q. Li, T. Y. Zhai, *Small* **2019**, 15, 18.
- [4] a) Q. H. Wang, K. Kalantar-Zadeh, A. Kis, J. N. Coleman, M. S. Strano, *Nat. Nanotechnol.* **2012**, 7, 699; b) L. Li, Y. Yu, G. J. Ye, Q. Ge, X. Ou, H. Wu, D. Feng, X. H. Chen, Y. Zhang, *Nat. Nanotechnol.* **2014**, 9, 372; c) H. Liu, A. T. Neal, Z. Zhu, Z. Luo, X. F. Xu, D. Tománek, P. D. Ye, *ACS Nano* **2014**, 8, 4033; d) D. Xiang, C. Han, J. Wu, S. Zhong, Y. Y. Liu, J. D. Lin, X. A. Zhang, W. P. Hu, B. Özyilmaz, A. H. C. Neto, A. T. S. Wee, W. Chen, *Nat. Commun.* **2015**, 6, 8; e) D. J. Perello, S. H. Chae, S. Song, Y. H. Lee, *Nat. Commun.* **2015**, 6, 7809; f) F. Xia, H. Wang, Y. Jia, *Nat. Commun.* **2014**, 5, 4458.
- [5] D. Li, M. Y. Chen, Z. Z. Sun, P. Yu, Z. Liu, P. M. Ajayan, Z. X. Zhang, *Nat. Nanotechnol.* **2017**, 12, 901.
- [6] F. Liu, X. Lin, Y. Yan, X. Gan, Y. Cheng, X. Luo, *Nano Lett.* **2023**, 23, 11645.
- [7] D. Li, M. Chen, Q. Zong, Z. Zhang, *Nano Lett.* **2017**, 17, 6353.
- [8] a) F. Gong, W. Deng, Y. Wu, F. Liu, Y. Guo, Z. Che, J. Li, J. Li, Y. Chai, Y. Zhang, *Nano Res.* **2024**, 17, 3113; b) Z. Peng, L. Tong, W. Shi, L. Xu, X. Huang, Z. Li, X. Yu, X. Meng, X. He, S. Lv, G. Yang, H. Hao, T. Jiang, X. Miao, L. Ye, *Nat. Commun.* **2024**, 15, 8650.
- [9] B. W. H. Baugher, H. O. H. Churchill, Y. F. Yang, P. Jarillo-Herrero, *Nat. Nanotechnol.* **2014**, 9, 262.
- [10] M. Buscema, D. J. Groenendijk, G. A. Steele, H. S. J. van der Zant, A. Castellanos-Gomez, *Nat. Commun.* **2014**, 5, 4651.
- [11] Q. R. Deng, T. Zhao, J. L. Zhang, W. B. Yue, L. Li, S. S. Li, L. Y. Zhu, Y. M. Sun, Y. Pan, T. Zheng, X. T. Liu, Y. Yan, N. J. Huo, *ACS Nano* **2024**, 18, 23702.
- [12] C. Liu, X. Yan, X. Song, S. Ding, D. W. Zhang, P. Zhou, *Nat. Nanotechnol.* **2018**, 13, 404.
- [13] M. S. Choi, G.-H. Lee, Y.-J. Yu, D.-Y. Lee, S. Hwan Lee, P. Kim, J. Hone, W. J. Yoo, *Nat. Commun.* **2013**, 4, 1624.
- [14] A. J. Hong, E. B. Song, H. S. Yu, M. J. Allen, J. Kim, J. D. Fowler, J. K. Wassei, Y. Park, Y. Wang, J. Zou, R. B. Kaner, B. H. Weiller, K. L. Wang, *ACS Nano* **2011**, 5, 7812.
- [15] W. Li, J. Y. Li, T. H. Mu, J. Y. Li, P. C. Sun, M. J. Dai, Y. H. Chen, R. J. Yang, Z. Chen, Y. C. Wang, Y. P. Wu, S. X. Wang, *Small* **2024**, 20, 13.
- [16] E. X. Wu, Y. Xie, S. J. Wang, D. H. Zhang, X. D. Hu, J. Liu, *Nanoscale* **2020**, 12, 18800.
- [17] a) E. X. Wu, Y. Xie, J. Zhang, H. Zhang, X. D. Hu, J. Liu, C. W. Zhou, D. H. Zhang, *Sci. Adv.* **2019**, 5, 9; b) F. K. Wang, K. Pei, Y. Li, H. Q. Li, T. Y. Zhai, *Adv. Mater.* **2021**, 33, 27.
- [18] a) J. J. Zha, S. H. Shi, A. Chaturvedi, H. X. Huang, P. Yang, Y. Yao, S. Y. Li, Y. P. Xia, Z. M. Zhang, W. Wang, H. D. Wang, S. C. Wang, Z. Yuan, Z. B. Yang, Q. Y. He, H. L. Tai, E. H. T. Teo, H. Y. Yu, J. C. Ho, Z. R. Wang, H. Zhang, C. L. Tan, *Adv. Mater.* **2023**, 35, 12; b) G. H. Lee, Y. J. Yu, C. Lee, C. Dean, K. L. Shepard, P. Kim, J. Hone, *Appl. Phys. Lett.* **2011**, 99, 3.
- [19] Y.-N. Xu, W. Y. Ching, *Phys. Rev. B* **1991**, 44, 7787.
- [20] a) M. Lenzlinger, E. H. Snow, *IEEE Trans. Electron Devices* **1968**, 15, 686; b) D. Qiu, D. U. Lee, K. S. Lee, S. W. Pak, E. K. Kim, *Nano Res.* **2016**, 9, 2319.
- [21] a) W. Liu, J. H. Lv, L. Peng, H. W. Guo, C. Liu, Y. L. Liu, W. Li, L. F. Li, L. X. Liu, P. Q. Wang, S. C. Bodepudi, K. Shehzad, G. H. Hu, K. H. Liu, Z. P. Sun, T. Hasan, Y. Xu, X. M. Wang, C. Gao, Y. Bin, X. F. Duan, *Nat. Electron.* **2022**, 5, 281; b) W. Wang, Y. Meng, W. Wang, Z. Zhang, P. Xie, Z. Lai, X. Bu, Y. Li, C. Liu, Z. Yang, S. Yip, J. C. Ho, *Adv. Funct. Mater.* **2022**, 32, 2203003.
- [22] a) J. Huang, K. Shu, N. Bu, Y. Yan, T. Zheng, M. Yang, Z. Zheng, N. Huo, J. Li, W. Gao, *Sci. China Mater.* **2023**, 66, 4711; b) Z. Liu, H. Liu, M. Zhang, L. Han, N. Huo, Z. Zheng, W. Gao, J. Li, M. Yang, *ACS Appl. Mater. Interfaces* **2024**, 16, 63752; c) Z. Li, T. Zheng, M. Yang, Y. Sun, D. Luo, W. Gao, Z. Zheng, J. Li, *Adv. Opt. Mater.* **2024**, 12, 2400023.
- [23] a) T. Zheng, M. Yang, Y. Pan, Z. Zheng, Y. Sun, L. Li, N. Huo, D. Luo, W. Gao, J. Li, *ACS Appl. Mater. Interfaces* **2023**, 15, 29363; b) C. Tan, H. Wang, X. Zhu, W. Gao, H. Li, J. Chen, G. Li, L. Chen, J. Xu, X. Hu, L. Li, T. Zhai, *ACS Appl. Mater. Interfaces* **2020**, 12, 44934; c) Y. Li, J.

Xiao, X. Cao, Z. Gu, W. Zhang, *Adv. Funct. Mater.* **2023**, *33*, 2213385; d) C. Zhang, S. Peng, J. Han, C. Li, H. Zhou, H. Yu, J. Gou, C. Chen, Y. Jiang, J. Wang, *Adv. Funct. Mater.* **2023**, *33*, 2302466; e) L. Tong, C. Su, H. Li, X. Wang, W. Fan, Q. Wang, S. Kunsági-Máté, H. Yan, S. Yin, *ACS Appl. Mater. Interfaces* **2023**, *15*, 57868; f) T. Bu, X. Duan, C. Liu, W.

Su, X. Hong, R. Hong, X. Zhou, Y. Liu, Z. Fan, X. Zou, L. Liao, X. Liu, *Adv. Funct. Mater.* **2023**, *33*, 2305490; g) C. H. Lee, Y. Park, S. Youn, M. J. Yeom, H. S. Kum, J. Chang, J. Heo, G. Yoo, *Adv. Funct. Mater.* **2021**, *32*, 2107992.
[24] Z. Wang, Q. Li, Y. Chen, B. Cui, Y. Li, F. Besenbacher, M. Dong, *NPG Asia Mater.* **2018**, *10*, 703.